Chapter 9
The Intermittency of ISM Turbulence: What Do the Observations Tell Us?

Edith Falgarone, Giorgos Momferratos, and Pierre Lesaffre

Abstract The interstellar medium is highly turbulent, but this medium, a partially ionized plasma, is also multi-phase, compressible and magnetized, hence the complexity of its turbulence extends beyond theoretical grasp. Turbulence being with gravity a key player in the star formation process, it is anticipated that its dissipation is a key process too. A fundamental property of turbulent dissipation is its space-time intermittency, studied mostly in hydrodynamical turbulence. After an overview of our limited knowledge of intermittency based on laboratory experiments, theory and numerical simulations, this chapter gathers the set of observations, now made possible by the new capabilities of molecular spectroscopy and polarimetry, that may be seen as signatures of intermittency in the magnetized turbulent interstellar medium. It includes powerful statistical approaches of the interstellar velocity field, the detection of large velocity-shears at very small scales, and chemical and radiative diagnostics of intermittent dissipation. Models of magnetized dissipation bursts, either in the form of coherent vortices or low velocity C-shocks are also presented and confronted to observations, as well as results on the regions of most intense dissipation in spectral simulations of magneto-hydrodynamical (MHD) and non-ideal turbulence.

9.1 The Turbulent Interstellar Medium

The interstellar medium (ISM) contributes to less that 1 % to the mass of our Galaxy (and in most galaxies of the present day universe) and yet it is the reservoir of gas that still allows the formation of new stars. It is paradoxical that this medium plays such a critical role in the cycle of cosmic matter and yet contributes such a small fraction of the galaxy masses. It is part of an open cycle that drives baryons from dying stars to new stars, at a rate of a few $M_\odot$ year^{-1} in our Galaxy, comparable to the rate of gas infall from the extragalatic environment. The warmest phases of the ISM are fully ionized. Its neutral and coldest phases, which comprise the bulk of its

E. Falgarone (✉) • G. Momferratos • P. Lesaffre
Ecole Normale Supérieure, 24 rue Lhomond, 75005 Paris, France
e-mail: edith.falgarone@ens.fr; giorgos.momferratos@ens.fr; pierre.lesaffre@ens.fr

mass, consist in two main phases, the cold neutral medium (CNM) at $\sim$100 K and the warm neutral medium (WNM) at $\sim$10^4 K, approximately in thermal pressure equilibrium (Field et al. 1969).

Because it sits in the gravitational potential of the Galaxy and it extends up to 1 kpc or more above the plane, the ISM has to be supported by a pressure that is about ten times its thermal pressure, $P_{tot} = 3 \times 10^{-12}$ dynes cm^{-2}, or $P_{tot}/k_B \sim 2 \times 10^4$ K cm^{-3} (Cox 2005). The non-thermal contributions to the total pressure are due to supersonic turbulence and magnetic fields, in rough equipartition, as shown by measurements of magnetic field intensity (Crutcher et al. 2010) and HI linewidths (Haud and Kalberla 2007). The distribution of thermal pressures in the Solar Neighbourhood, inferred from [CI] fine-structure absorption lines towards nearby stars (Jenkins and Tripp 2011) peaks at about $P_{th}/k_B \sim 3 \times 10^3$ K cm^{-3}, with large fluctuations, up to a few 10^4 K cm^{-3}. It is noteworthy that the total non-thermal pressure in the Galactic plane is of the same order as the largest thermal pressure fluctuations observed, suggesting that the non-thermal energy eventually and occasionally degrades into thermal energy.

Interstellar turbulence has been advocated very early (von Weizsäcker 1951) but the nature, origin and properties of turbulence in the ISM are still highly debated and controversial issues in spite of dedicated observational and numerical efforts. Moreover, the gas suprathermal motions might just be random motions if a full turbulent cascade does not have time to develop in the violent ISM. We recall here a few definitions.

The definition of turbulence is built on experiment. Turbulence is an instability of laminar flows. Their velocity field $\mathbf{u}$ satisfying the incompressibility condition $\nabla \cdot \mathbf{u} = 0$ is solution of the Navier–Stokes equation

$$\partial_t \mathbf{u} + (\mathbf{u} \cdot \nabla)\mathbf{u} = -\frac{\nabla p}{\rho} + \nu \nabla^2 \mathbf{u} \qquad (9.1)$$

where p is the pressure and ν is the kinematic viscosity. This instability develops as soon as the inertial $\mathbf{u} \cdot \nabla \mathbf{u}$ accelerations greatly exceed the viscous $\nu \Delta \mathbf{u}$ ones (ν is the kinematic viscosity) i.e. when the Reynolds number $Re = lu_l/\nu$, at a scale l of characteristic velocity u_l, exceeds a few hundreds. This instability at scale l is at the origin of an energy transfer to smaller scales, that eventually become unstable too and transfer their kinetic energy to still smaller scales, etc... This is the turbulent cascade that develops between the integral scale, L, at which energy is injected, and the dissipation scale l_D, close to the particle mean-free-path, where energy is dissipated into heat due to the particle viscosity. The timescale for the growth of this instability is of the order of the turnover time $\tau_l = l/u_l$ at each length scale l. Kolmogorov (1941) (hereafter K41) predicted the self-similar behavior of the velocity field in incompressible turbulence by postulating a dissipationless cascade characterized by a transfer rate of kinetic energy independent of scale, $\epsilon_l \propto u_l^2/\tau_l = u_l^3/l$, hence the well-known scaling $u_l \propto l^{1/3}$. It is easy to demonstrate that this assumption leads to an energy spectrum $E(k) \propto k^{-5/3}$ known as the Kolmogorov spectrum. $E(k)$ has the dimension of a kinetic energy per unit mass and

Table 9.1 Characteristics of the turbulence observed in various components of the interstellar medium (Solar Neighborhood). ϵ_l is expressed in $L_\odot/M_\odot$ for comparison with the energy provided by stellar radiation

		CNM	Molecular clouds	Low-mass dense cores
$\overline{n}$	cm^{-3}	30	200	10^4
l	pc	10	3	0.1
T	K	100	20	10
σ_l	km s^{-1}	≈ 3.5	1	0.1
B	μG	10	20	100
$\mathbf{v}_A$	km s^{-1}	3.4	2	1.4
$\epsilon_l = \frac{1}{2}u_l^3/l$	$L_\odot/M_\odot$	10^{-3}	10^{-4}	10^{-6}
$\epsilon_\rho = \frac{1}{2}\overline{\rho}u_l^3/l$	erg cm^{-3}s^{-1}	2×10^{-25}	1.7×10^{-25}	2.5×10^{-25}
Λ	erg cm^{-3}s^{-1}	5×10^{-24}	4×10^{-24}	3×10^{-24}
$P_{turb} = \frac{1}{3}\overline{\rho}u_l^2$	erg cm^{-3}	3×10^{-11}	2×10^{-11}	10^{-11}
$\nu = \frac{1}{3}\lambda u_{th}$	cm^2 s^{-1}	2.2×10^{17}	1.5×10^{16}	2.1×10^{14}
$l_d = (\nu^3/\epsilon_l)^{1/4}$	AU	3.2	0.8	0.1
$Re = lu_l/\nu$		7.6×10^7	9.6×10^7	2.3×10^7

unit wavenumber because the average specific kinetic energy at scale $l = 2\pi/k$ is $\langle u_l^2 \rangle = \int_k^\infty E(k')dk'$. In Kolmogorov turbulence, the turnover timescale τ_l therefore decreases towards small-scales while the velocity gradient $u_l/l \propto l^{-2/3}$ increases. In the case of the ISM, the Reynolds numbers in the neutral ISM (see Table 9.1) are $\sim 10^8$ and the turnover timescale of the largest scales (300 pc, the thickness of the HI disk, and 6 km s^{-1}, the cloud velocity dispersion) is of the order of 50 Myr. It may be seen as the largest time required for the turbulent cascade to develop. We thus consider that in the bulk of the ISM (far from regions actively forming young stars) a turbulent cascade has time to develop and the gas motions are truly turbulent. Interestingly, the energy spectrum of mildly supersonic turbulence (rms sonic Mach numbers ~ 1) has a slope comparable to that of the Kolmogorov spectrum, and this holds for decaying (Porter et al. 1998), driven (Porter et al. 2002) hydrodynamic turbulence, as well as MHD turbulence (Vestuto et al. 2003). This is so because, after a few turnover times, the power in compressible modes drops below that in solenoidal (or shear) modes, whatever the initial conditions, amounting to no more than $\sim 10\%$ of the total power. In MHD turbulence, the relative power of shear to compressible modes increases as the magnetic field intensity increases (Vestuto et al. 2003).

The difficulty at characterizing interstellar turbulence is due in part to the huge range of scales separating those of the energy injection, at the Galaxy scale and even beyond when extragalactic infall is taken into account (see de Avillez and Breitschwerdt 2005), from those where it is dissipated, presumably below the milliparsec scale. It is also due to the fact that the turbulence is compressible, magnetized and multi-phase. It is critical, though, to unravel the properties of interstellar turbulence because turbulence and magnetic fields are the main contributions to the pressure of the ISM and the main stabilizing support of molecular clouds against

their self-gravity. Turbulent dissipation is therefore a key process among those leading to the formation of molecular clouds, star formation, and therefore galaxy evolution (see the reviews of Elmegreen and Scalo 2004; Scalo and Elmegreen 2004; Hennebelle and Falgarone 2012).

Studies of a turbulent velocity field are by nature statistical and in the case of the ISM have to rely on the analysis of line shapes observed at high spectral resolution. Early works were conducted on large samples of absorption lines observed against nearby stars. The λ 21 cm line of atomic hydrogen is hard to interpret because of the mixture of emission from the WNM and self-absorption by the CNM. However, a remarkable Kolmogorov spectrum covering two orders of magnitude in scales has been obtained in a high-latitude region where the HI emission arises primarily in the CNM (Miville-Deschênes et al. 2003a). The high optical depth of the ^{12}CO(1-0) line has opened new fields of investigation of the turbulence within molecular clouds. Molecular clouds, as seen in this line, have the remarkable property that their CO line emission is "clumpy" at all scales, i.e. the CO line intensity highly fluctuates in space and velocity, a property likely due to the underlying turbulence. The pioneering Larson's study (1981) who ascribed to turbulence the power-law increase $\propto l^{0.38}$ of the internal velocity dispersion of clouds of size l has now been extended to larger samples of molecular clouds and tracers. We refer to Hennebelle and Falgarone (2012) for references and a critical review of these results.

CO(1-0) observations provide a measurement of the kinetic energy transfer rate per unit volume $\epsilon_\rho = \frac{1}{2}\rho u_l^3 / l$ where ρ and $u_l = 1.6\sigma_l$ are the mean gas density and mean velocity of scale l, respectively. The large fluctuations of this quantity in a population of molecular clouds traced by ^{12}CO(1-0) are in sharp contrast with the fact that its *average* value stays the same from structures of 0.01 pc to giant molecular clouds (GMC) of 100 pc and has the value observed in the atomic gas (Haud and Kalberla 2007) (see Fig. 6 in Hennebelle and Falgarone 2012). This suggests that ϵ_ρ is an invariant of the hierarchy of molecular clouds traced by CO(1-0) and that these clouds are part of the same turbulent cascade as the atomic ISM. The energy spectrum in molecular gas is therefore expected to differ from the Kolmogorov spectrum. Note however that the average density between the smallest (10^{-2} pc) and largest (100 pc) scales increase only by a factor of 20. The Kolmogorov spectrum obtained in the nearby CNM (Miville-Deschênes et al. 2003a) is due to the fact that the CNM density does not fluctuate much: its thermal pressure is well defined (Jenkins and Tripp 2011) alike its temperature $T_K \sim 80$ K inferred from HI absorption measurements.

The characteristics of interstellar turbulence as observed in the diffuse medium (HI in emission), molecular clouds and dense cores (see Table 9.1) are such that the possible invariant of the cascade, the energy transfer rate ϵ_ρ, encompasses the warm neutral medium and the coldest and densest structures of low-mass ($M \leq$ a few M$_\odot$). If we assume that the energy transfer rate equals the average dissipation rate in the cascade, the comparison of $\epsilon_\rho \sim 10^{-25}$ erg cm^{-3}s^{-1} and Λ, the average cooling rate, in Table 9.1, shows that turbulent dissipation is too low, on average, to be a dominant source of heating of the ISM, in comparison with that provided by starlight (> 1 L$_\odot$/M$_\odot$). Turbulent dissipation may however become a dominant

heating source locally, if it is concentrated in bursts that fill only a small subset of space. This is the property of space-time intermittency of turbulence that is discussed in this chapter.

9.2 Intermittency in Hydrodynamical Incompressible Turbulence

9.2.1 Definitions and Statistical Signatures

For half a century now, turbulence has been recognized to be intermittent i.e. the smaller the scale, the larger the spatio-temporal velocity fluctuations, relative to their average value. Turbulent energy is not evenly distributed in space and time by the turbulent cascade: at each step of the cascade, the active sub-scales do not fill space so that the subset of space on which the active scales are distributed has a multifractal geometry (see the review of Anselmet et al. 2001 and the book of Frisch 1996). The statistical properties of the velocity fluctuations have been widely studied experimentally in laboratory and atmospheric flows: in all cases, the statistics of *velocity derivative and increments* signals are found to be non-Gaussian, with large departures from the average more frequent than for a Gaussian distribution. The probability distribution function (*pdf*) of the turbulent velocity field, in turn, remains Gaussian. Moreover, the departure of the *velocity increments pdf*s from a Gaussian distribution increases as the lag over which the increments are measured decreases. All the functions of the velocity involving a spatial derivative have therefore non-Gaussian *pdf*s: the velocity shears ($\partial_j u_i$) and, accordingly, the rate-of-strain $S_{ij} = \partial_j u_i + \partial_i u_j$ and the dissipation rate in incompressible turbulence $\epsilon_D = \frac{\nu}{2} \Sigma_{ij} (\partial_j u_i + \partial_i u_j)^2$, with non-Gaussian wings more pronounced at small scale.

The quantitative signature of intermittency appears in the behavior of the high-order structure functions of the longitudinal velocity field measured over a lag s, $\langle [\delta u_x(s)]^p \rangle \propto s^{\zeta_p}$. This relation is statistical, not deterministic, and the brackets hold for an average over an "appropriate" volume with respect to s^3. The anomalous scaling of the exponents $\zeta_p \neq p/3$ characterizes the degree of intermittency and provides the multifractal dimension of the most singular structures, i.e. that of the subset of space where the smallest active regions, and turbulent dissipation, are distributed (Anselmet et al. 2001). In incompressible turbulence, the so-called *active small scales* are those of largest vorticity or velocity shear. Various models have been proposed for the values of ζ_p. The most successful is certainly the one proposed by She and Lévêque (1994) who infer the relation

$$\zeta_p = \frac{-\gamma + 1}{3} p + \gamma \frac{1 - \beta^{p/3}}{1 - \beta}, \tag{9.2}$$

where γ is the exponent of the dissipation rate scaling in regions containing the most intermittent structures and β is related to the co-dimension C of the strongest dissipation structures $\gamma/(1-\beta) = C$. For incompressible hydrodynamical turbulence, the dissipative structures tend to be filamentary with co-dimension $C = 3-1 = 2$ while $\gamma = 2/3$ is assumed to be valid for the most dissipative structures. In compressible turbulence, where dissipation occurs in shocks (Boldyrev et al. 2002), and magnetized turbulence where it occurs in current sheets (Politano and Pouquet 1995; Müller and Biskamp 2000), the most intense dissipative structures are two-dimensional, so that the co-dimension $C = 1$ while $\beta = 1/3$ (see Pan et al. 2008).

Another essential facet of turbulent intermittency is that the most active small scales are not randomly distributed in space but are organized into coherent structures—*the sinews of turbulence*, as qualified by Moffatt et al. (1994). In incompressible turbulence, the structures of largest vorticity and weak rate-of-strain ($S_{ij} = \partial_j u_i + \partial_i u_j$) tend to be filamentary, while those of highest rate-of-strain and dissipation are rather in the form of sheets or ribbons, following the analysis of numerical simulations (Roux et al. 1999; Moisy and Jiménez 2004). These structures are remarkable in the sense that they are both large scales, i.e. their length is comparable to the integral scale of turbulence, and small scale structures, i.e. they have substructure down to the dissipation scale. The coupling between the largest and smallest scales operated by turbulence is now well established in simulations, as shown by Mininni, Alexakis and Pouquet who find that small-scale intermittency is more pronounced in turbulent fields where the large-scale shear is larger (Mininni et al. 2006a).

9.2.2   Open Questions

The above section has not addressed some fundamental facets of intermittency: the multifractal nature of the subset of space on which turbulent dissipation is concentrated, the link between intermittency of the velocity and that of the dissipation, and the duality of the Eulerian and Lagrangian descriptions of intermittency. These facets have been studied in incompressible hydrodynamical (HD) flows and, interestingly, the results point towards the existence of a universal behaviour. In their analysis of laboratory experiments monitoring the fluctuations of pressure in a turbulent flow, Roux et al. (1999) have shown that once they have removed the strong signals associated with intense vorticity filaments the multifractal nature of the background pressure fluctuation persists, providing strong experimental support to the multifractal distribution of the pressure fluctuations. In a joint analysis of the best available laboratory and numerical experiments at high Reynolds numbers, Arnéodo and his team (Arnéodo et al. 2008) show that the multifractal description captures intermittency at all scales, including the dissipative range, with only a few parameters independent of Re. They provide a unifying description of the scalings of the Lagrangian and Eulerian velocity structure functions. Chevillard et al. (2013) further develop the phenomenology of intermittency in the Lagrangian context,

using new experimental and numerical results. They find that the multifractal formalism captures the universality of intermittency, down to the dissipative scales and in the Eulerian and Lagrangian frames.

Whether or not the universality of HD turbulence in a broad range of Re numbers is relevant to more complex turbulent fields, such as ISM turbulence, is an open question. It is encouraging though that the Lagrangian velocity fluctuations are found to be highly intermittent too because, as will be seen below, it strengthens the possibility that intermittent dissipation of turbulence impacts the chemistry of the gas phase.

9.3 Intermittency in the ISM: The Observers Perspective

Searches for non-Gaussian statistics in the ISM velocity field have been conducted for many years now and some results are presented below. Measurements of the departure of the moments of order p of the velocity structure functions from the $\zeta_p = p/3$ prediction of the K41 model are extremely difficult in practice because the number of independent measurements needed to compute S_p grows as $\sim 10^{p/2}$. Access to $p = 8$, for instance, therefore requires 10^4 independent measurements. In the ISM, only recently has this been accessible.

9.3.1 Signatures of the Intermittency in the Velocity Field of Molecular Clouds

#### 9.3.1.1 Parsec-Scale Coherent Structures of Intense Velocity-Shear

Identifying regions of intermittency in interstellar turbulence is challenging for several independent reasons. Firstly, these regions are non-space filling and correspond to rare events in time and space: their finding requires the analysis of large homogeneous statistical samples of the velocity field. This means observations at high spectral and spatial resolution of large regions of interstellar material. Secondly, observations do not provide the full velocity field, but only its line-of-sight (*los*) projection provided by the Doppler-shift of a molecular line, so statistical analysis similar to those performed in laboratory flows or in the solar wind are not possible. However, measurements of the spectrum of molecular lines with a frequency resolution finer than the sound speed in cold H_2 provide information on the suprathermal velocity field. The ^{12}CO(1-0) line has turned out to be a most useful tool for this search.[1] Thirdly, only spatial variations of the *los* velocity in the plane-

---

[1] under the restriction that only diffuse molecular gas of low to moderate line opacity be studied, to avoid complications due to radiative transfer.

of-the-sky (*pos*) are provided by observations. Therefore, the velocity variations are by essence cross-variations $\partial_j u_i$. Finally, the line emission being integrated along a *los*, the velocity information at a given position is the full line profile and its moments, the first moment being the line centroid velocity C. The statistics of the velocity increments are built through those of the line centroid velocity increments (CVI) δC_l measured between two positions separated by a lag l in the *pos*. The CVIs have been shown by Lis et al. (1996) to be a proxy of extrema of vorticity, being the *los* average of the *pos* projection of the vorticity. This is because the vorticity is a signed quantity. In the *los* integration, the vorticity fluctuations cancel out and the result is dominated by a few large values, when they exist.

Thanks to the improved efficiency of observations at high spectral resolution in the millimeter wave domain, it is now possible to map large fields at high spectral and spatial resolutions with a high sensitivity in a reasonable amount of observing time. An example, drawn from observations in the Polaris Flare carried out at the IRAM-30 m telescope in the ^{12}CO($J = 2 - 1$) line, is shown in Fig. 9.1 (Hily-Blant and Falgarone 2009). The $\sim 10^5$ independent spectra sample homogeneous turbulence in diffuse molecular gas. The CVI-*pdf*s in that field have the anticipated non-Gaussian wings that increase as the lag over which the increment is measured decreases (Fig. 9.2, left). The locus of the extreme CVIs (the E-CVIs) that build
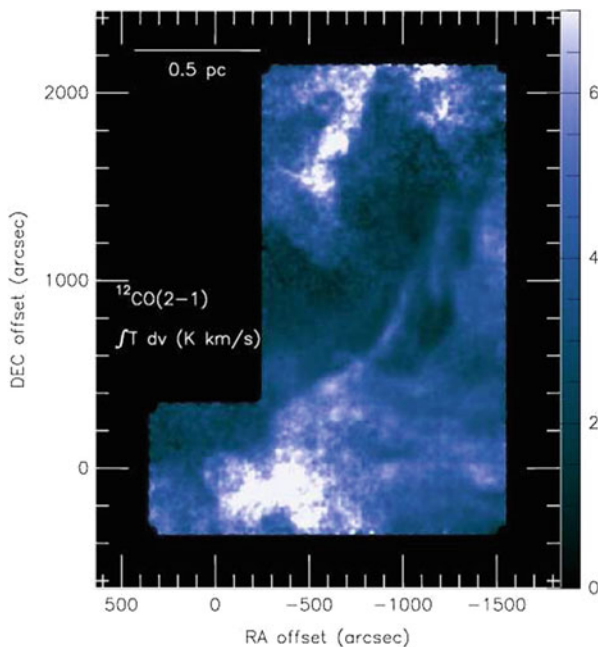
Fig. 9.1 Map of the ^{12}CO(J=2-1) integrated intensity (in K km s^{-1}) over a $40' \times 30'$ area located in the Polaris Flare. The number of independent spectra is $\sim 10^5$. The spatial resolution is 11 arcsec or 8 mpc at the distance of the field, d=150 pc
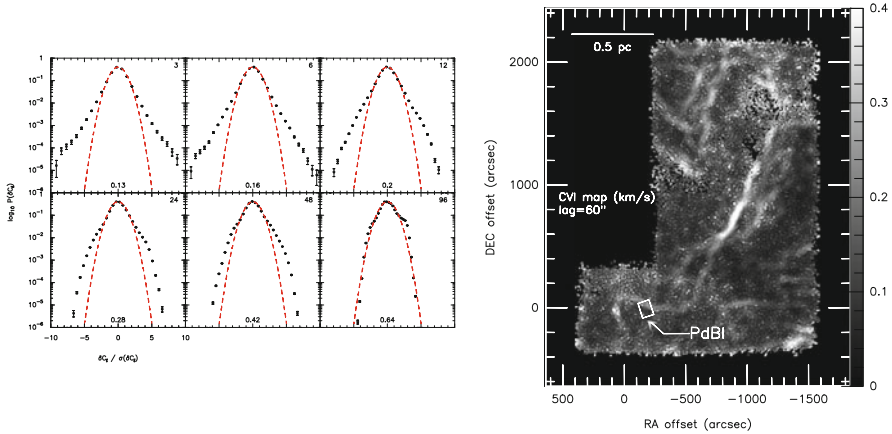
Fig. 9.2 *Left*: Normalized *pdf*s of line centroid velocity increments δC_l measured over variable lags, expressed in units of 15 arcsec (numbers in the *upper right* corners), and computed within the field of Fig. 9.1. The Gaussians of same dispersion $\sigma(\delta C_l)$ (given in km s^{-1} at the *bottom* of each panel) are also drawn. The non-Gaussian wings of the *pdf*s increase as the lag decreases. Note that, as expected, a probability of 10^{-5} is reached in the most extreme bins. *Right*: In the same field, locus of the positions populating the non-Gaussian wings of the *pdf* for a lag of 60 arcsec. The wedge is in km s^{-1}. The rectangle locates the area observed with the IRAM-PdBI. From Hily-Blant and Falgarone (2009)

up the non-Gaussian wings of the *pdf*s is an elongated narrow structure ($\sim$0.03 pc thick), almost straight over more than one parsec and surrounded by an ensemble of weaker, shorter structures (Fig. 9.2, right). As expected, the lane of largest E-CVIs coincides with the region where the velocity-shears are the largest, 40 km s^{-1} pc^{-1} (see Hily-Blant and Falgarone 2009). Most interestingly, it also coincides with a lane of weak ^{12}CO(2-1) emission and one of the weakest filaments of dust thermal emission detected at 250 μm in that field with *Herschel*/SPIRE (Miville-Deschênes et al. 2010). Last, two low-mass dense cores lie at the South-East tip of the E-CVIs locus (Heithausen et al. 2002). All these suggest a *causal link* between extrema of turbulent dissipation, the formation of CO molecule, the formation of tenuous dense filaments and that of low-mass dense cores.

A similar analysis has been performed in a cloud edge of the Perseus–Taurus–Auriga giant molecular complex. The field has the same total hydrogen column density as that in the Polaris Flare, but is less turbulent (half the pc-scale rms velocity dispersion). The CVI-*pdf*s show departures from a Gaussian distribution with an amplitude 2.5 times smaller than in the Polaris Flare (Hily-Blant et al. 2008). This result is in agreement with the theoretical predictions of Mininni et al. (2006a) and further supports the fact that these observations are manifestations of intermittency.

These properties taken together, (1) the increasing departure of CVI-*pdf*s from a Gaussian distribution as the scale decreases, (2) the spatial coherent structures of E-CVIs and (3) the link between the large-scale properties of turbulence and the magnitude of the small-scale E-CVIs, all suggest that the ^{12}CO(2-1) E-CVIs

trace the intermittency of turbulence in diffuse molecular clouds. The multifractal geometry of the E-CVIs structures in the Polaris Flare probed by the non-linear dependence of ζ_p with p up to $p = 6$ discussed in Hily-Blant et al. (2008) is now confirmed, up to higher orders, by the analysis of this larger data set. Unexpectedly, the ζ_p departure from a linear dependence agrees, within the error bars, with the predictions for incompressible turbulence (She and Lévêque 1994). Hily–Blant, Falgarone and Pety also show the sharp increase of the flatness (or kurtosis) of the velocity field, defined here as $\frac{\langle \delta C_l^4 \rangle}{\langle \delta C_l^2 \rangle^2}$ as the scale l decreases (Hily-Blant et al. 2008).

9.3.1.2 Milliparsec-Scale Observations: Approaching the Dissipation Scales

A step further towards small-scales is provided by IRAM Plateau de Bure Interferometer (PdBI) ^{12}CO(1-0) line observations of the small field shown in Fig. 9.2 (right) at a resolution of $\sim$4 arcsec or 3 mpc (Falgarone et al. 2009). These observations are unique so far: the lines detected are very weak, but the spatial dynamic range of the map is large enough to allow the detection of eight elongated structures with thickness as small as $\approx$3 mpc (600 AU) and length up to 70 mpc, set indeed by the size of the field. They are *not filaments* because once merged with short-spacing data, the PdBI-structures appear to be the sharp edges of more extended CO emission. Moreover, six out of eight form pairs of quasi-parallel structures at different velocities. Statistically, this cannot be due to chance alignment. Velocity-shears estimated for the three pairs include the largest values ever measured in non-star-forming regions, up to 780 km s^{-1} pc^{-1}. Other cases of CO(1-0) milliparsec-scale structures forming elongated patterns with large velocity-shear (up to $\sim$180 km s^{-1} pc^{-1}) have been found in diffuse gas (Heithausen 2006, 2004). Finally, the PdBI-structures are almost straight and their different position angles, cover a broad range of values, from $PA = 60°$ to $165°$, an unexpected result given the small size of the field. The scatter of their PAs is therefore as large within that small field of $\sim$70 mpc than it is for the coherent structure in the parsec-scale field (Fig. 9.2).

9.3.1.3 Polarization Measurements of Starlight in the Polaris Flare

Dust absorption polarizes starlight and the direction of the polarization turns out to be that of the *pos* projection of the magnetic field, B_{pos}, because dust grains are aligned by the magnetic field by processes that we do not detail here (see the chapter of Andersson, this volume, for a review). The sampling of the field direction is therefore uneven and dictated by the position of the background stars bright enough to allow measurements of polarized light that amounts to only a few % of the star luminosity. The Polaris Flare has been observed in the visible (Mohan et al., in prep.) with the "Beauty and the Beast" spectro-polarimeter at Mt Megantic (Manset and

Bastien 1995) over a large field of $\sim$30 pc, providing 45 sensitive measurements, the polarization fractions measured being as low as 0.3 %. The distribution of the *PA*s of the polarization at large scale is broad, with values distributed from 10° to 150°. In the near-IR, observations have been carried out with the Mimir imaging polarimeter (Clemens et al. 2012) at the Perkins telescope of two $10' \times 10'$ (or 0.45 pc) fields encompassing the PdBI-field and the area of largest E-CVIs (Fig. 9.2, right). The number of detected polarizations barely exceeds ten because at these high latitudes the number of stars bright enough to perform polarization measurements is low. However, the scatter of the *PA*s is as large as that observed at the 30 pc-scale and there is a trend for the *pos* projection of the magnetic field to be aligned with the intense velocity-shears. Yet, any statistically meaningful comparison of the orientation of B_{pos} with the structures of most intense velocity shears has to rely on more observations.

These results on intense velocity-shears and starlight polarization do not provide a full three-dimensional view of the magnetic fields in regions of velocity-shear extrema, but they carry promising information. The regions of intense velocity-shears are straight structures in projection in the *pos* at the arcmin-scale ($\sim$0.05 pc) (Falgarone et al. 2009). They have to be straight also in real space and therefore be part of sheets that are straight in at least one direction. This is reminiscent of the findings of Mininni, Pouquet and Montgomery regarding the formation of parallel current and vortex sheets in MHD turbulence that destabilize, fold and roll up along directions parallel to the magnetic fields (Mininni et al. 2006b). We put these results in perspective of pseudo-spectral numerical simulations of non-ideal magnetized turbulence in Sect. 9.5.

9.3.2   Signatures of Intermittency: Hot Glitters in the Cold Medium

A resilient and major puzzle has long been the existence in the diffuse ISM of molecular species that have a formation endothermicity far above the available thermal energy: their large observed abundances cannot be reproduced by state-of-the-art chemistry models driven by UV photons and cosmic-rays only (Le Petit et al. 2006). This has been known for 70 years in the case of CH^+ that was among the first molecular species discovered in space by absorption spectroscopy against nearby stars. Not only does this cation form through the highly endothermic reaction $C^+ + H_2$ ($\Delta E / k = 4940$ K) but it is also rapidly destroyed by collisions with H_2. The puzzle has been recently deepened and extended to the whole Galaxy by *Herschel*/HIFI observations of the $CH^+ (J = 1 - 0)$ transition in absorption against the dust continuum emission of remote star forming regions (Falgarone et al. 2010a,b), confirming the very high abundance of this cation in the diffuse ISM. Similarly, SH^+, that has a formation endothermicity almost twice as large as CH^+, is also observed to be abundant in the diffuse ISM (Menten et al. 2011; Godard et al. 2012).

Another outstanding and more recent puzzle is the origin of the H_2 pure rotational line emission of the diffuse ISM. Its discovery dates back to the ISO-SWS detection of the four lowest rotational transitions across a large pathlength of diffuse gas in the Galactic plane, $N_H \sim 10^{22}$ cm^{-2}, equivalent to 16 mag (Falgarone et al. 2005). Given the high energy of the upper level of these transitions, 510 K for the S(0) line, up to 2,540 K for the S(3) line, and the absence of intense UV radiation field able to excite these levels by fluorescence, a non-thermal excitation of some kind is required. This Galactic emission was modelled by advocating heating of the gas by turbulent dissipation. The dissipation regions, distributed along the line of sight, were either hundreds of low velocity magneto-hydrodynamical (MHD) shocks (8–12 km s^{-1}) or thousands tiny regions of intense velocity-shears, heating the gas by ion-neutral friction and/or viscous dissipation. The interesting new result of these models was that a fraction as small as a few percent of warm gas, heated by dissipation of mechanical energy, was sufficient to reproduce the observed line intensities, and their line ratios. New detections of these lines have been performed by *Spitzer*/IRS, in the diffuse gas around supernova remnants (Hewitt et al. 2009), at an edge of the Taurus molecular complex (Goldsmith et al. 2010), and in several diffuse clouds (Ingalls et al. 2011). In all these studies, UV excitation cannot explain the H_2 line intensities and non-thermal excitation, likely fed by turbulent dissipation, is required.

Last, large fluctuations of the CO emission of diffuse gas at small scale have been observed that cannot be ascribed to UV-shielding fluctuations (see references in Hennebelle and Falgarone 2012). This sharp variability is primarily due to CO chemistry, a point that cannot be understood in the framework of UV-driven chemistry and is discussed in the next section.

9.4 Intermittency in the ISM: The Theoretical Chemistry Perspective

Models of non-equilibrium chemistry have attempted to capture the essence of the coupling between the impulsive heating due to intermittent turbulent dissipation and the warm chemistry it triggers. They have focussed on the diffuse ISM because it is there that the very first steps of chemistry in space take place with the formation of the light hydrides, formed by reaction of the most abundant heavy elements (C, O, N, S, Si) with H_2. It is there too that the high observed abundances of these light hydrides cannot be understood. This is so because many of the formation reactions of these hydrides are so highly endothermic that they are blocked at the temperature of the cold diffuse ISM that contains the traces of H_2 indispensable for the chemistry to be initiated. Table 9.2 gives the broad range of energy barriers that the chemistry of light hydrides offers. The presence of these species in the cold ISM can thus be used as diagnostics of intermittent dissipation of turbulence. Two different frameworks have been adopted for the dissipative structures: either small-scale magnetized vortices (Joulain et al. 1998; Godard et al. 2009) or magnetized low-

Table 9.2 Non-exhaustive list of bottleneck reactions for molecule formation with their temperature barrier or endothermicity

Reaction	Temperature barrier (K)
$O + H_2 \rightarrow OH + H$	2,980
$C^+ + H_2 \rightarrow CH^+ + H$	4,640
$S + H_2 \rightarrow SH + H$	9,620
$S^+ + H_2 \rightarrow SH^+ + H$	9,860
$C + H_2 \rightarrow CH + H$	14,100
$Si^+ + H_2 \rightarrow SiH^+ + H$	14,310
$N + H_2 \rightarrow NH + H$	14,600
H_2 dissociation energy	52,000

velocity shocks (Falgarone et al. 2005; Lesaffre et al. 2013). They are discussed below.

9.4.1   Non-Equilibrium Chemistry in a Magnetized Burgers Vortex

The TDR model (for Turbulent Dissipation Regions model Godard et al. 2009, 2012, 2014), is based on the fact that turbulent dissipation that involves $\nabla \cdot \mathbf{u}$ and $\nabla \times \mathbf{u}$ is an intermittent quantity. It is built on an analytical solution of the Helmholtz equation for the vorticity, the Burgers vortex. In addition to the traditional parameters of chemistry models, the density n_H and UV shielding characterized by the visual extinction A_V, the free parameters of the TDR model are constrained by the known large-scale properties of turbulence in the diffuse medium (see Joulain et al. 1998): the rate-of-strain a—a quantity homogeneous to s^{-1}—(see definition in Sect. 9.2) and the maximum orthoradial gas velocity in the vortex, set by the turbulent velocity dispersion at large scale. The rate-of-strain and the equilibrium radius of the vortex are related by $r_0^2 = 4\nu/a$. A hydrodynamical steady-state of a (slightly modified) magnetized Burgers vortex of finite length is computed. The gas density is low enough that the neutral component decouples from the ions and magnetic field in the layers where the orthoradial velocity is the largest. The thermal and chemical evolution of a fluid cell crossing the steady-state vortex is computed in a Lagrangian frame. The dissipation is due to (1) viscous dissipation in the layers of intense velocity-shear at the vortex outer boundary and (2) ion-neutral friction induced by the decoupling of the ionized and neutral flows in the central regions.

Since the diffuse medium has a low density, its chemical and thermal inertia are large. The TDR model takes into account the long-lasting relaxation period that follows the end of any dissipative burst. The vortex lifetime, i.e. the duration of the burst of dissipation, is set by energetic considerations (see Godard et al. 2009, 2014) and is as short as a few hundred years. A random line of sight through the medium therefore samples three kinds of gas: thousands of active vortices occupying at most a few percent of any random line of sight across the medium, many more relaxation

phases and the ambient medium. The relaxation times of the different species cover a broad range, from 200 year for CH^+ up to 5×10^4 year for CO. This introduces a potentially untractable complexity in the comparison of the abundances of different species.

A large number of models have been run to explore the parameter space varying the density ($30 < n_H < 500$ cm^{-3}), the visual extinction ($0.1 < A_V < 2$ mag), the rate-of-strain ($10^{-12} < a < 10^{-10}$ s^{-1}) and the average turbulent energy transfer rate, ϵ, assumed to be equal to the average dissipation rate $\overline{\epsilon}_D$.

The main results are as follows (Godard et al. 2014):

1. The CH^+ abundance is found to increase linearly with $\overline{\epsilon}_D$, which makes this radical a specific tracer of the dissipation of suprathermal energy in the ISM. The observed abundances of CH^+ and SH^+ are well reproduced for the conditions prevailing in the diffuse ISM in the Galaxy, including the inner Galaxy.
2. The efficient formation of CH^+ opens a new branch of chemical reactions by producing CH_3^+, a daughter species of CH^+. CH_3^+ is very reactive and for instance, by reaction with O, forms HCO^+, a parent species of CO. The warm chemistry driven by turbulent dissipation therefore produces many daughter-species and significantly contributes to the formation of CO in the diffuse turbulent medium.
3. The observed abundances tend to favor low rates-of-strain, i.e. models in which dissipation is dominated by ion-neutral friction rather than viscous dissipation. Remarkably, the pc-scale velocity shear of 40 km s^{-1} pc^{-1} observed in the Polaris Flare would correspond to a straining field from the large scales $a = 1.5 \times 10^{-12}$ s^{-1}, while the intense small-scale shear of 780 km s^{-1} pc^{-1} detected at the mpc-scale is 20 times larger. Both rates-of-strain are in the range of a values consistent with chemical observations.
4. Only a few percent of the gas heated by turbulent dissipation are sufficient to trigger the warm chemistry consistent with observations.
5. The last interesting prediction of the TDR model is the intensity of the radiative cooling during the thermal relaxation phase. It is dominated by the H_2 pure rotational lines, as long as the gas temperature is above ~ 500 K, then, as the gas cools down, the fine-structure [CII] and OI lines take over. It is remarkable that the total energy radiated by H_2 and C^+ during the relaxation phase is about the same, the latter being about ten times weaker on average over a duration ten times larger. The [CII] emission from a gas component heated by turbulent dissipation rather than by UV photons is predicted to be a possible significant fraction of the total [CII] emission of the diffuse medium.

9.4.2 Non-equilibrium Chemistry in Magnetized Shocks

Another dissipative process in supersonic turbulence occurs in shocks. Shocks are anticipated to be part of the grand pattern of intermittent dissipation of

ISM turbulence. We discuss below models of the non-equilibrium chemistry that develops in low-velocity C-type shocks. They have specific features that can be used to estimate the degree of magnetization of the medium for instance.

When two parcels of fluid collide with relative velocities greater than the information propagation speed, a shock is born. From a large scale point of view, the shock looks like a thin sheet, or working surface, where the relative kinetic energy between the fluid parcels is converted to magnetic, radiative, thermal and internal energy. The surge of thermal energy at the working surface can trigger chemical reactions otherwise blocked by thermal barriers. In the reference frame of the working surface, the gas flows into the shock from one side (the pre-shock) and flows out from the other side (the post-shock side). The entrance velocity of the shock is defined as the velocity of the fluid in the pre-shock side relative to the speed of the working surface. In a magnetized and partially ionised gas such as the ISM, two information speeds are relevant. The fastest speed is the magnetosonic speed in the ionized fluid and the slowest is the Alfvén speed in the neutral gas.

When the shock speed is greater than both these speeds, a J-type shock occurs where ions and neutrals remain coupled at all times. The fine structure of the shock inside the working surface is as follows (see Fig. 9.3). At the shock entrance, kinetic energy is converted on a few mean free paths (i.e. the viscous length) by viscous friction into heat and internal energy. Gradual cooling ensues which depends on the chemical composition of the gas. This converts thermal energy into radiation and the decrease of temperature leads to an increase of density. Indeed, because of the increased temperature, the sound speed is now very large, and the working surface is very nearly uniform in pressure, so density and temperature are related. This
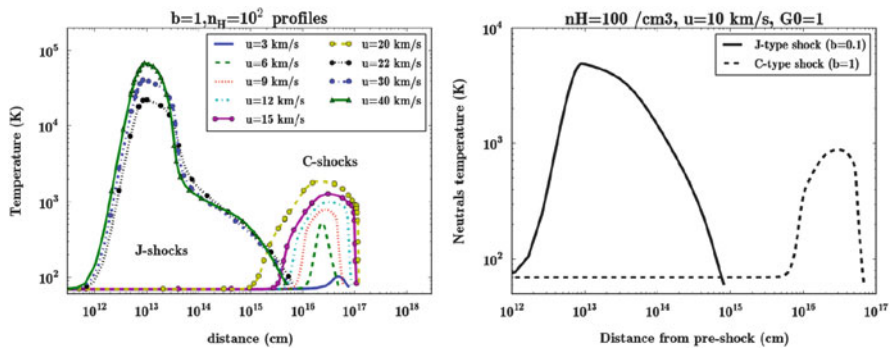
Fig. 9.3 *Left*: Temperature profiles for highly magnetized shocks ($b = 1$) of different velocities u. Here $b = B/n_{\mathrm{H}}^{-0.5}$ with B expressed in μG and n_{H} in cm^{-3}. The fluid flows from *left to right* with the preshock on the *left* and post-shock on the *right*. Only J-type shocks are present for the lowest values of the b/u ratio. *Right*: Temperature profiles for two different magnetizations ($b = 0.1$ and 1) and one shock velocity. It displays the relevant lengthscales: the viscous length that extends to $d = 10^{13}$ cm from pre-shock, the cooling length that ends at $d = 10^{15}$ cm, which is roughly the thickness of the J-type shock, the ion-neutral coupling length $d = 5 \times 10^{16}$ cm at which ions and neutrals start to recouple and the heating due to ion-neutral friction starts to drop. From Lesaffre et al. (2013)

compression leads to field lines compression and part of the input energy through the shock is converted into magnetic energy.

When the shock speed is greater than the Alfvén speed in the neutrals but lower than the magnetosonic speed in the ions, ions and neutrals experience the shock differently. The information propagates faster than the shock speed in the ions, which just experience a wave, whereas the neutrals experience a shock. The resulting structure at the beginning is a J-type shock with a continuous magnetic precursor upstream. The relative speed between the ions and neutrals leads to friction which tends to recouple the two fluids and in most cases, the J-type shock eventually disappears to leave only a continuous structure known as a C-type shock. Across the working surface, friction between ions and neutrals now mediates the conversion of kinetic energy into heat. In this case the heating, the cooling and magnetic compression all happen at the same time. The resulting temperature is lower than for corresponding J-type shocks, with lower final compression factors, but the thickness of the working surface is much greater than for a J-type shock. Indeed, the length of a J-type shock is controlled by the cooling length of the gas, whereas in a C-type shock the gas cannot cool until the ion and neutral velocities are recoupled (see Fig. 9.3, right), and it is the much longer ion-neutral coupling lengthscale which dictates the width of the shock. As a result, the total column-densities across C-type shocks are usually higher than for J-type shocks. Hence, the impact on some chemical tracers in the gas can actually be much greater and each type of shock has its own specific chemical signature (Lesaffre et al. 2013; Flower and Pineau des Forêts 2012).

The components of the magnetic field relevant for the computation of the above information speeds are the components which lay in the shock surface. In a turbulent medium it is likely that the orientation of the field with respect to the normal of the shock surface can be arbitrary and both types of shocks are likely to co-exist. Moreover, the velocity vector is not necessarily orthogonal to the working surface, thus leading to oblique shocks. Oblique shocks lead to a rotation of the transverse component of the magnetic field when crossing the working surface (Pilipp and Hartquist 1994). To conclude, although the orientation of both the velocity and the magnetic fields vectors with respect to the shock surface both matter, it is nevertheless hard to infer any correlations between the shock orientation and the magnetic fields.

The chemical yields from magnetized shocks may be attributed to several factors. First, the increase of temperature due to the dissipation which helps to increase the chemical rates: it does so drastically when the reactions are subject to thermal barriers comparable to the temperature obtained in these shocks (see Table 9.2). Second, the compression which increases the collisional rates and shortens the chemical time-scales. Third, the drift velocity which provides additional energy in the reference frame for the ion-neutral reactions. The first factor acts in both types of shocks, the second one operates mainly in J-type shocks and the third one exclusively in C-type shocks. This diversity of factors implies a variety of chemical signatures for J-type and C-type shocks (see Lesaffre et al. 2013). For example, CO, OH and H_2O are enhanced in both types of shock, but require higher

velocities for C-type shocks than J-type shocks. Conversely, CH^+ relies on ion-neutral reactions and its abundance is increased more in C-type shocks than in J-type shocks.

9.5 Intermittency in MHD and Non-ideal Turbulence: The Theorist and Numericist Perspectives

Turbulence in a magnetized ionized fluid exhibits fundamentally different dynamics from that in neutral fluids. There is not even agreement among theorists on the energy spectrum of MHD turbulence. The discussions in Wan et al. (2012), Beresnyak (2011), Mason et al. (2012) illustrate recent advances in this controversy (see also the chapter by Beresnyak and Lazarian in this volume). Yet, intermittency has been advocated in a number of magnetized turbulent environments. For example, Schmidt et al. (2010) have shown that the treatment of intermittency in supernovae explosions may play a crucial role. In another context, the formation of chondrules in meteorites requires an intermittent heating which may be a signature of the turbulent state of the Solar Nebulae at the time (King and Pringle 2010). Below, we recall some fundamental properties of magnetized turbulence. We also report on ongoing numerical efforts at characterizing dissipation in spectral simulations of MHD and non-ideal turbulence by Momferratos et al. (2014).

9.5.1 Energy Spectrum

The incompressible MHD equations read

$$\partial_t \mathbf{u} + (\mathbf{u} \cdot \nabla) \mathbf{u} = -\frac{\nabla p}{\rho} + \mathbf{j} \times \mathbf{b} + \nu \nabla^2 \mathbf{u} \qquad (9.3)$$

$$\partial_t \mathbf{b} + \nabla \times (\mathbf{u} \times \mathbf{b}) = \eta \nabla^2 \mathbf{b} \qquad (9.4)$$

where $\mathbf{u}$ is the velocity field satisfying $\nabla \cdot \mathbf{u} = 0$, $\mathbf{b} = \mathbf{B}/\sqrt{4\pi\rho}$ is the Alfvén velocity in a fluid of density ρ satisfying $\nabla \cdot \mathbf{b} = 0$, p is the pressure, $\mathbf{j} = \nabla \times \mathbf{b}$ is the current density, ν is the kinematic viscosity and η is the magnetic diffusivity. If $\nu = \eta = 0$, the above system conserves total energy $E = 1/2\langle \mathbf{u}^2 \rangle + 1/2\langle \mathbf{b}^2 \rangle$, cross-helicity $H_c = \langle \mathbf{u} \cdot \mathbf{b} \rangle$ and magnetic helicity $H_m = \langle \mathbf{a} \cdot \mathbf{b} \rangle$ where $\mathbf{a}$ is the vector potential, $\mathbf{b} = \nabla \times \mathbf{a}$.

In the presence of a mean magnetic field $\mathbf{B}_0$, the introduction of the Elsässer variables $\mathbf{z}^\pm = \mathbf{u} \pm \mathbf{b}$ leads to the following symmetric form of the MHD equations

$$\partial_t \mathbf{z}^\pm \mp (\mathbf{v}_A \cdot \nabla)\mathbf{z}^\pm + (\mathbf{z}^\mp \cdot \nabla) \mathbf{z}^\pm = -\nabla p^* + \nu^+ \nabla^2 \mathbf{z}^\pm + \nu^- \nabla^2 \mathbf{z}^\mp \qquad (9.5)$$

where $\mathbf{v}_A = \mathbf{B}_0/\sqrt{4\pi\rho}$ is the Alfvén velocity of the mean field, $p^* = p/\rho + b^2/2$ is the total pressure and $2v^\pm = v \pm \eta$. The second term on the left hand side represents counter-propagating Alfvén waves. The difference in sign between the two equations implies that the mean magnetic field cannot be canceled by a Galilean transformation, and is thus dynamically important at all scales. The next term corresponds to nonlinear interaction of Alfvén waves through collisions.

Total energy and cross-helicity can be expressed in terms of the Elsässer variables as $E = \langle (\mathbf{z}^+)^2 \rangle$ and $H_c = \langle (\mathbf{z}^-)^2 \rangle$. This implies that two colliding Alfvén waves are deformed by the non-linear term in such a way that the above quantities remain constant, since they are only dissipated by the diffusive terms.

This property allowed Iroshnikov and Kraichnan (IK) (Iroshnikov 1963; Kraichnan 1965) to construct a phenomenological theory of the inertial range. If the Alfvén wave amplitude at a scale λ is δu_λ, during a collision of two waves it changes by the magnitude of the nonlinear term $\delta u_\lambda^2/\lambda$ multiplied by the interaction time λ/v_A: $\Delta \delta u_\lambda = \delta u_\lambda^2/\mathrm{v}_A$. If one further assumes that collisions change the energy of the waves as a random walk, the number of collisions required to deform each wave considerably is $N = (\delta u_\lambda/\Delta \delta u_\lambda)^2 = (\mathrm{v}_A/\delta u_\lambda)^2$. The timescale of the cascade is $\tau_{IK} = N\lambda/\mathrm{v}_A = (\lambda \mathrm{v}_A)/\delta u_\lambda^2$. Assuming a constant energy flux through the inertial range $\varepsilon = \delta u_\lambda^2/\tau_{IK}$, one obtains the scaling $\delta u_\lambda \propto \lambda^{1/4}$. The energy spectrum $E(k) \propto | \delta u_k^2 | k^2$ scales as $k^{-3/2}$ in the inertial range.

In the IK theory, the energy spectrum is isotropic. Goldreich and Sridhar (GS) (Goldreich and Sridhar 1995) introduced the assumption of critical balance: the Alfvén term $\mp(\mathbf{v}_A \cdot \nabla)\mathbf{z}^\pm$ is of the same order as the nonlinear term $(\mathbf{z}^\mp \cdot \nabla)\mathbf{z}^\pm$. This implies $\mathrm{v}_A/l \sim \delta b_\lambda/\lambda$ with l the longitudinal scale of the wave and λ its transverse scale. l is equal to the product of the Alfvén velocity v_A and the eddy turnover time $\tau_{GS} = \lambda/\delta u_\lambda$, implying $\delta u_\lambda \sim \delta b_\lambda$. τ_{GS} is chosen as the timescale of the cascade, and the constancy of the energy flux $\delta u_\lambda^2/\tau_{GS}$ gives $\delta u_\lambda \sim \delta b_\lambda \propto \lambda^{1/3}$ in the inertial range. This scaling is identical to K41, except that the scale λ is perpendicular to the magnetic field, resulting in an anisotropic energy spectrum $E(k_\perp) \propto k_\perp^{-5/3}$. In fact, critical balance implies $l \propto \lambda^{2/3}$, so that the cascade becomes increasingly anisotropic at small scales.

9.5.2 Intermittency in MHD Turbulence

In MHD turbulence, the energy dissipation rate

$$\varepsilon = \frac{v}{2} \sum_{i,j=1}^{3} \left(\partial_i u_j + \partial_j u_i \right)^2 + \eta \left(\nabla \times \mathbf{b} \right)^2 \tag{9.6}$$

includes the Ohmic dissipation in addition to the viscous dissipation. It is found to be concentrated largely on two-dimensional structures. These sheets of dissipation are observed in spectral simulations of incompressible MHD turbulence (Fig. 9.4,
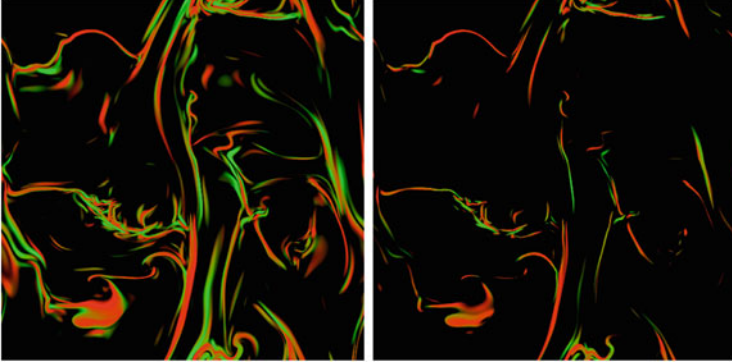
Fig. 9.4 Color maps of dissipation field at the temporal peak of total dissipation for the ABC initial conditions and two different ranges of the total dissipation (see Fig. 9.5): between the mean value μ and $\mu + \sigma$ (*left panel*) and between $\mu + \sigma$ and $\mu + 3\sigma$ (*right panel*). The subset of space on which dissipation is concentrated is much less space-filling for the higher dissipation rates. *Red*: Ohmic dissipation, *green*: viscous dissipation. From Momferratos et al. (2014)

Momferratos et al. 2014). Spectral methods are known to be of very high accuracy and well-suited for the study of small-scale structure (Canuto and Funaro 1988). The simulation is a freely decaying solution of Eqs. (9.3) and (9.4) with a null mean magnetic field. Two different initial conditions were considered for the large scale flow: one based on the Arnol'd–Beltrami–Childress (ABC) flow and the other based on the Orszag–Tang (OT) vortex. In the case of the ABC initial conditions, the non-dimensional cross-helicity

$$H_c = \frac{2\langle \mathbf{u} \cdot \mathbf{b} \rangle}{\sqrt{\langle \mathbf{u}^2 \rangle \langle \mathbf{b}^2 \rangle}} \tag{9.7}$$

is $\sim 2 \times 10^{-3}$, corresponding to a low initial correlation between the velocity field and the magnetic field. The mean magnetic helicity

$$H_m = \langle \mathbf{a} \cdot \mathbf{b} \rangle \tag{9.8}$$

where $\mathbf{a}$ is the vector potential with $\mathbf{b} = \nabla \times \mathbf{a}$, is considerable, $H_m \sim 0.2 u_0^2 l_0$. Here, l_0 and u_0 are typical length and velocity scales of the simulations. In the case of the OT initial conditions, the non-dimensional cross-helicity is ~ 0.1 while the mean magnetic helicity is almost zero, $H_m \sim 1 \times 10^{-9} u_0^2 l_0$. Thus, these two different initial conditions represent evolution under different constraints. Yet, the dissipation fields, such as that shown in Fig. 9.4 for the ABC initial conditions, are qualitatively very similar. The *pdf* of the total dissipation exhibits a log-normal core and a power-law tail that corresponds to extreme heating events. It is shown in Fig. 9.5 for the ABC initial conditions.

Fig. 9.5 *Pdf* of the total dissipation rate for the ABC initial conditions at the temporal peak of total dissipation rate. μ is the mean and σ the standard deviation. From Momferratos et al. (2014)
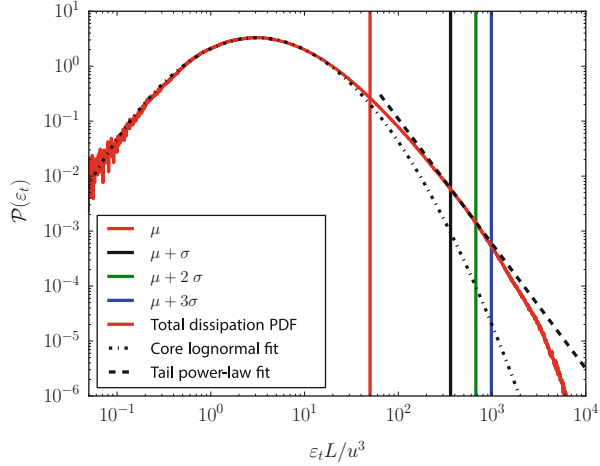
Just as in HD turbulence, intermittency can be quantified by the deviation of the scaling exponents of the velocity field and magnetic field structure functions from the K41 values. In the inertial range $l_D \ll r \ll L$, they scale as $S_p^{\{u,b\}}(r) \propto r^{\zeta_p^{\{u,b\}}}$. The intermittency model of She and Lévêque (1994) was generalized by Politano and Pouquet (1995) taking into account different possibilities for the co-dimension of the structures of high dissipation C and the scaling exponent of the increments in the inertial range $\delta u_\lambda \sim \delta b_\lambda \propto \lambda^{1/g}$

$$\zeta_p^{GSL}(g, C) = \frac{p}{g}\left(1 - \frac{2}{g}\right) + C\left(1 - \left(1 - \frac{2}{gC}\right)^{\frac{p}{g}}\right) \qquad (9.9)$$
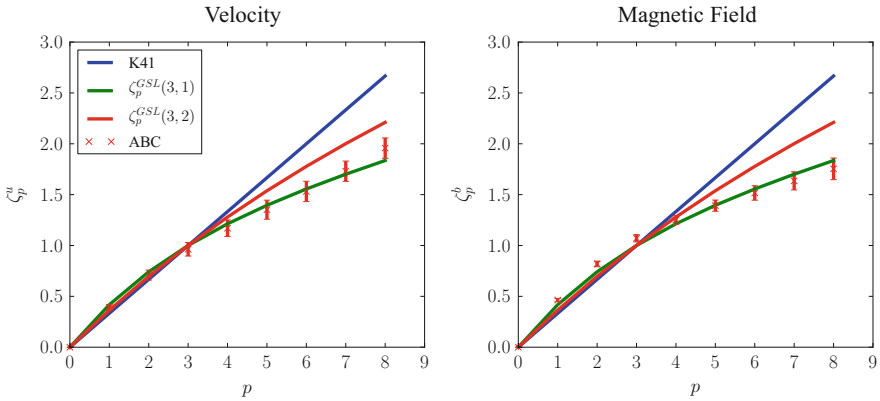
where GSL stands for the generalized She-Lévêque model. The co-dimension $C = 1$ for sheets, while the scaling parameter g is 3 for K41 and 4 for IK.

The method of extended self-similarity (ESS) introduced by Benzi et al. (1993) facilitates the estimation of structure function exponents from experimental or numerical data by extending the range of scales where their value is constant. This method considers the relative exponent

$$\frac{\zeta_p^u}{\zeta^*} = \frac{d \log(S_u^p(r))}{d \log(S^*(r))} \qquad (9.10)$$

where the scaling of the structure function $S^*(r)$ is known from theory. In MHD, $S^*(r)$ is provided by the four-thirds law of Politano and Pouquet (1998)

$$S_3^\pm(r) = \langle \delta \mathbf{z}_\parallel^\pm (\delta \mathbf{z}^\mp)^2 \rangle = -\frac{4}{3}\langle \varepsilon^\pm \rangle r, \quad l_D \ll r \ll L \qquad (9.11)$$

Fig. 9.6 Velocity and magnetic field structure function exponents for the ABC initial condition, calculated using extended self-similarity. The curves corresponding to two cases of the generalized She-Lévêque model, labelled by the scaling parameter g and the co-dimension C are drawn as well as the K41 linear dependence

where ε^+ is the energy dissipation and ε^- is the cross-helicity dissipation. This is an exact statistical result which follows from the MHD equations under the assumptions of statistical homogeneity, isotropy, stationarity and zero magnetic helicity (Politano and Pouquet 1998). Figure 9.6 displays the structure function exponents for the same ABC simulation, calculated up to order eight using ESS. The results agree quite well with the generalized She-Lévêque model, under the assumptions that the structures of high dissipation are sheets and that in the inertial range the scaling exponent of the increments is $1/3$. The magnetic field is found to be more intermittent than the velocity field, its exponents having a larger deviation from the K41 non-intermittent prediction.

The tail of the *pdf* of the total dissipation, shown in Fig. 9.5, corresponds to extreme dissipation events that have a complex geometrical structure. Following Uritsky et al. (2010), Momferratos et al. (2014) have defined the structures of high dissipation as connected sets of points each having a local value of the total dissipation above a prescribed threshold. The structures of high dissipation exhibit varied geometrical complexity, but are overall quasi two-dimensional, i.e. sheet-like. A statistical analysis shows that their geometric and dynamical characteristics exhibit power-law scaling, with different exponents in the inertial and dissipative ranges (Uritsky et al. 2010; Momferratos et al. 2014).

As a last illustration of the high degree of spatial intermittency observed in simulations of MHD turbulence, Momferratos et al. (2014) show that the curve giving the fraction of total dissipation contained in structures that take up a given volume fraction rises very steeply near the origin. As a result, 30 % of the total dissipation is contained in less than 3 % of the total volume.

9.5.3 Intermittency in Non-ideal Turbulence: Ambipolar Diffusion

In the diffuse interstellar medium, the partially ionized state of the gas can have significant effects on the turbulent motions. The most complete description of the motion of a partially ionized gas is the two fluid model (see the chapter of Zweibel, this volume). In the diffuse ISM however, for low ionization fractions, ρ_i/ρ_n, one can neglect ion inertia, pressure and viscosity and assume that in the ion momentum equation, the friction force due to the ion-neutral drift is balanced by the Lorentz force. If one further assumes incompressibility, the equations of ambipolar diffusion MHD reduce to the following system:

$$\partial_t \mathbf{u} + (\mathbf{u} \cdot \nabla) \mathbf{u} = -\frac{1}{\rho}\nabla p + \mathbf{j} \times \mathbf{b} + \nu \nabla^2 \mathbf{u} \tag{9.12}$$

$$\partial_t \mathbf{b} = \nabla \times (\mathbf{u} \times \mathbf{b}) + (\gamma \rho_i)^{-1} \nabla \times \big((\mathbf{j} \times \mathbf{b}) \times \mathbf{b}\big) + \eta \nabla^2 \mathbf{b} \tag{9.13}$$

where $\mathbf{b} = \mathbf{B}/\sqrt{4\pi\rho}$ is the Alfvén velocity defined in terms of the total density $\rho = \rho_n + \rho_i$ and γ is the coefficient of ion-neutral friction.

Equations (9.12) and (9.13) were simulated using the same spectral method as in the pure MHD case described in the previous section by Momferratos et al. (2014), with identical initial conditions to compare the evolution with and without ambipolar diffusion.

Ambipolar diffusion has a significant effect on the spatial structure of the dissipation field. In a partially ionized gas, in addition to viscous and Ohmic dissipation, total energy is also dissipated by ambipolar diffusion (or more correctly, by the friction between the ions and the neutrals) at the rate

$$\varepsilon_a = (\gamma \rho_i)^{-1} \left((\mathbf{j} \times \mathbf{b}) \times \mathbf{b}\right)^2 \tag{9.14}$$

The intermittent spatial structure of the dissipation field in the case of ambipolar diffusion is shown in Fig. 9.7 where two ranges of the total dissipation rate are selected: the larger the dissipation rate, the smaller the volume filling factor of the subset of space on which dissipation is distributed. Ambipolar diffusion contributes a more diffuse component to the dissipation field, that has the tendency to surround the sheets of Ohmic and viscous dissipation (see Momferratos et al. 2014 for a quantitative discussion). This is reminiscent of the early findings of Brandenburg and Zweibel (1994). The dissipation due to ion-neutral friction i.e. ambipolar diffusion) contributes significantly to extreme heating events because the power-law tail in the *pdf* of total dissipation is more pronounced in the case with ambipolar diffusion.

Last, Fig. 9.8 is an attempt at reproducing the quantities observable in the ISM with their unavoidable projections. A proxy of viscous dissipation, the contribution due to the *pos* projection of the vorticity is shown in the top panel. This quantity is close to the increments of the line centroid velocity that are accessible to
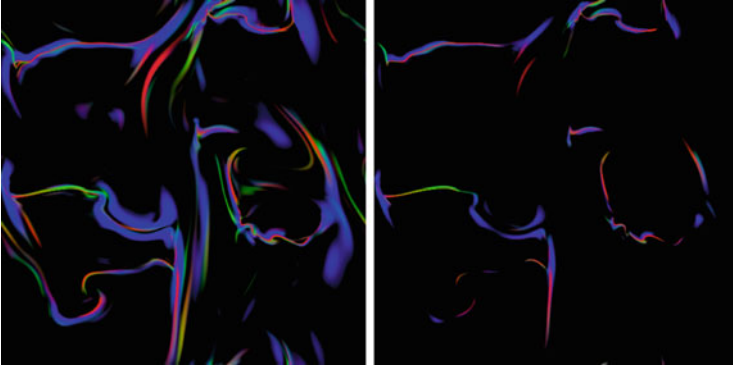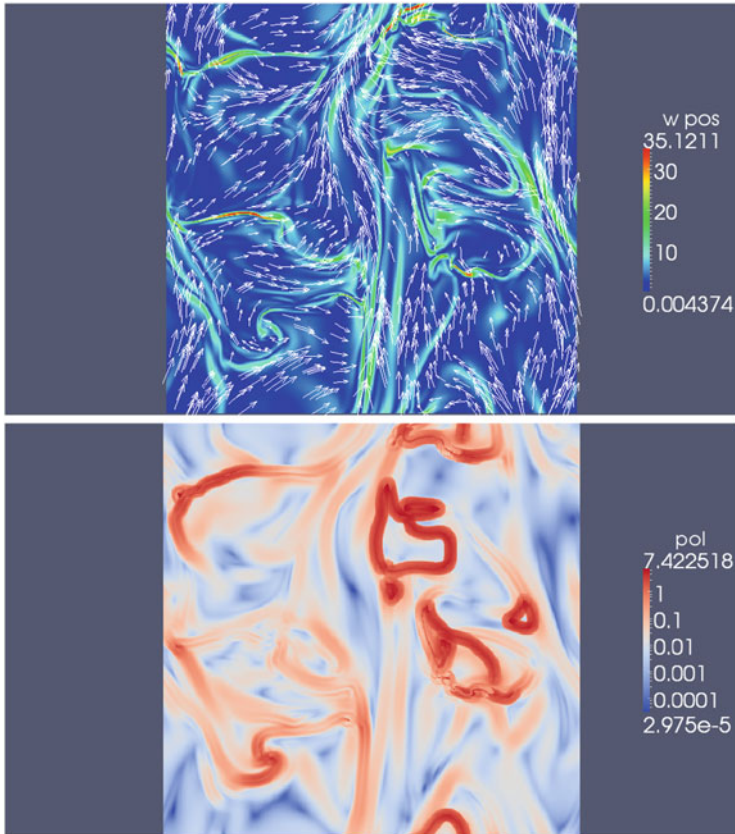
Fig. 9.7 Maps of the dissipation field in the ABC run with ambipolar diffusion, at the temporal peak of total dissipation. The same dissipation ranges as in Fig. 9.4 are shown: between the mean value μ and $\mu+\sigma$ (*left panel*) and between $\mu+\sigma$ and $\mu+3\sigma$ (*right panel*). *Red*: Ohmic dissipation, *green*: viscous dissipation, *blue*: dissipation due to ambipolar diffusion. The latter is distributed in thicker structures than those due to ohmic dissipation (*red*) and viscous dissipation (*green*)

observations (Sect. 9.3.1). The *pos* projection of the magnetic field is also shown. This projection is that provided by the measurements of the polarization angle of either the dust thermal emission (in which case the field direction is perpendicular to that of the polarization) or the absorbed starlight in the visible or near-IR (in which case the field direction is parallel to that of the polarization). The bottom panel displays $\Delta\Psi$, the increment of the orientation of B_{pos} averaged over annuli of ten resolution elements in radius. The comparison of the patterns visible in these figures with those of Fig. 9.7 shows that the largest *pos* projections of the vorticity and the largest $\Delta\Psi$ at small scale delineate structures that tend to follow those of the most intense dissipation, although it is not a one-to-one correspondence, due to projection effects. The same is true for the alignment of B_{pos} and the projected vorticity.

9.6   Summary and Perspectives

In spite of the theoretical and experimental challenges it poses, even in incompressible turbulence, and in spite of the lack of predictions in magnetized compressible turbulence, intermittency seems to be present in the ISM. It manifests itself by non-Gaussian statistics of the velocity field that are more salient at small scales and by the existence of coherent structures of velocity-shears over a broad range of scales (from pc to mpc scales). An indirect facet of its existence is the impact of intermittent turbulent dissipation that locally heats the ISM and opens chemical routes that are blocked by highly endothermic reactions in the cold ISM . These reactions have thresholds that span an extended range in energy so that chemistry

Fig. 9.8 Comparison of two proxies of observables of the dissipation field in the ABC simulation with weak ambipolar diffusion: the *pos* projection of the vorticity, a proxy of the line velocity centroid increments (see Sect. 9.3.1) (*top*), the small scale increments of the direction of the *pos* projection of the magnetic field, a proxy of the variations of the polarization angle of the dust thermal emission (*bottom*). The *pos* projections of the magnetic field are superposed in the *top panel*

could be envisioned as a test of the multifractal nature of intermittency: the molecular species with the highest barriers would be the tracers of the fractal set of smallest fractal dimension and largest local dissipation. From these signatures of intermittency in the chemistry of the diffuse ISM, we infer that Lagrangian intermittency is indeed present. Lagrangian intermittency would also impact the mixing of dynamical, thermal and dynamical properties of the gas and hence the transport processes.

As far as the magnetic field is concerned, only very few measurements are presently available in the field where the velocity field has been investigated with large enough statistics at small scales. There is, however, a possible trend of alignment of the vorticity and magnetic field in the plane-of-the-sky which needs

to be put on a firmer statistical basis. The topology of the smallest scale structures accessible to observations still escapes numerical grasp but the perspectives in the field of observations are bright.

Last, intermittency seems to be a universal phenomenon, present as soon as the Reynolds number is high enough, and it is likely to have an impact in a broad variety of astrophysical media ranging from the most dilute intergalactic medium to the densest stellar interiors, including all phases of the interstellar medium, protoplanetary discs and supernovae.

References

Anselmet, F., Antonia, R., Danaila, L.: Planet Space Sci. **49**, 1177 (2001)

Arnéodo, A., Benzi, R., Berg, J., et al.: Phys. Rev. Lett. **100**, 4504A (2008)

Benzi, R., Ciliberto, S., Baudet, C., Ruiz Chavarria, G., Tripiccione, R.: Phys. Rev. Lett. **48**, 29 (1993)

Beresnyak, A.: Phys. Rev. Lett. **106**, 075001 (2011)

Boldyrev, S., Nordlund, A., Padoan, P.: Astrophys. J. **573**, 678 (2002)

Brandenburg, A., Zweibel, E.G.: Astrophys. J. **427**, L91 (1994)

Canuto, C., Funaro, D.: SJNA, **25**, 24 (1988)

Chevillard L., Castaing, B., Arnéodo, A., Lévêque, E., Pinton J.-F., Roux, S.: CR Phy. **13**, 899C (2013)

Clemens, D.P., Pinnick, A.F., Pavel, M.D.: Astrophys. J. Suppl. **200**, 20 (2012)

Cox, D.: Ann. Rev. Astron. Astrophys. **43**, 337 (2005)

Crutcher, R., Wandelt, B., Heiles, C., Falgarone, E., Troland, T.: Astrophys. J. **725**, 466 (2010)

de Avillez, M., Breitschwerdt, D.: Astron. Astrophys. **436**, 585 (2005)

Elmegreen, B., Scalo, J.: Ann. Rev. Astron. Astrophys. **42**, 211 (2004)

Falgarone, E., Verstraete, L., Pineau Des Forêts, G., Hily-Blant, P.: Astron. Astrophys. **433**, 997 (2005)

Falgarone, E., Pety, J., Hily-Blant, P.: Astron. Astrophys. **507**, 355 (2009)

Falgarone, E., Ossenkopf, V., Gerin, M., et al. Astron. Astrophys. **518**, L118 (2010)

Falgarone, E., Godard, B., Cernicharo, J., et al.: Astron. Astrophys. **521**, L15 (2010)

Field G., Goldsmith, D., Habing, H.: Astrophys. J. **155**, 149 (1969)

Flower, D., Pineau des Forêts, G.: Mon. Not. R. Astron. Soc. **421**, 2786 (2012)

Frisch, U.: Turbulence. Turb. book. Cambridge, UK, Cambridge University Press, (1996)

Godard, B., Falgarone, E., Pineau des Forêts, G.: Astron. Astrophys. **495**, 847 (2009)

Godard, B., Falgarone, E., Gerin, M., et al.: Astron. Astrophys. **540**, 87 (2012)

Godard, B., Falgarone, E., Pineau des Forêts, G.: Astron. Astrophys. (2014, in press). arXiv1408. 3716G

Goldreich, P., Sridhar, S.: Astrophys. J. **438**, 763 (1995)

Goldsmith, P., Velusamy, T., Li, D., Langer, W.: Astrophys. J. **715**, 1370 (2010)

Haud, U., Kalberla, P.: Astron. Astrophys. **466**, 555 (2010)

Heithausen, A.: Astron. Astrophys. **606**, L13 (2004)

Heithausen, A.: Astron. Astrophys. **450**, 193 (2006)

Heithausen, A., Bertoldi, F., Bensch, F.: Astron. Astrophys. **383**, 591 (2002)

Hennebelle P., Falgarone, E.: Astron. Astrophys. Rev. **20**, 55 (2012)

Hewitt, J.W., Rho, J., Andersen, M., Reach, W.T.: Astrophys. J. **694**, 1266 (2009)

Hily-Blant, P., Falgarone, E.: Astron. Astrophys. **500**, L59 (2009)

Hily-Blant, P., Falgarone, E., Pety, J.: Astron. Astrophys. **481**, 367 (2008)

Ingalls, J., Bania, T., Boulanger, F., Draine, B., Falgarone, E., Hily-Blant, P.: Astrophys. J. **743**, 174 (2011)

Iroshnikov, P.: Sov. Astron. **7**, 566 (1963)

Jenkins, E., Tripp, T.: Astrophys. J. **734**, 65 (2011)

Joulain, K., Falgarone, E., Pineau des Forêts, G., Flower, D.: Astron. Astrophys. **340**, 241 (1998)

King, A.R., Pringle, J.E.: Mon. Not. R. Astron. Soc. **404**, 1903 (2010)

Kolmogorov A.N.: Proc. R. Soc. Lon. Ser. A **434**, Reprinted in 1991 (1941)

Kraichnan, R.: Phys. Fluids **8**, 1385 (1965)

Larson, R.: Mon. Not. R. Astron. Soc. **194**, 809 (1981)

Le Petit, F., Nehmé, C., Le Bourlot, J., Roueff, E.: Astrophys. J. Suppl. **164**, 506 (2006)

Lesaffre, P., Pineau des Forêts, G., Godard, B., et al.: Astron. Astrophys. **550**, A106 (2013)

Lis, D., Pety, J., Phillips, T., Falgarone, E.: Astrophys. J. **463**, L623 (1996)

Manset, N., Bastien, P.: Publ. Astron. Soc. Pac. **107**, 83 (1995)

Mason, J., Perez, J.C., Boldyrev, S., Cattaneo, F.: Phys. Plasmas **19**, 055902 (2012)

Menten, K., Wyrowski, F., Belloche, A., Güsten, R., Dedes, L., Müller, H.: Astron. Astrophys. **525**, 77 (2011)

Mininni, P.D., Alexakis, A., Pouquet, A.: Phys. Rev. Lett. **74**, 6303M (2006)

Mininni, P.D., Pouquet, A., Montgomery, D.C.: Phys. Rev. Lett. **97**, 4503M (2006)

Miville-Deschênes, M.-A., Joncas, G., Falgarone, E., Boulanger, F.: Astron. Astrophys. **411**, 109 (2003a)

Miville-Deschênes, M.-A., Martin, P., Abergel, A.: Astron. Astrophys. **518**, L104 (2010)

Moffatt, H., Kida, S., Ohkitani, K.: J. Fluid Mech. **259**, 241 (1994)

Moisy, F., Jiménez, J.: J. Fluid Mech. **513**, 111 (2004)

Momferratos, G., Lesaffre P., Falgarone, E., Pineau des Forêts, G.: Mon. Not. R. Astron. Soc. **443**, 86 (2014)

Müller, C., Biskamp, D.: Phys. Rev. Lett. **84**, 475 (2000)

Pan, L., Wheeler, J., Scalo, J.: Astrophys. J. **681**, 470 (2008)

Pilipp, W., Hartquist T.W.: Mon. Not. R. Astron. Soc. **267**, 801 (1994)

Politano, H., Pouquet, A.: Phys. Rev. Lett. **52**, 636 (1995)

Politano, H., Pouquet, A.: Phys. Rev. Lett. **57**, 21 (1995)

Porter, D.H., Woodward, P.R., Pouquet, A.: Phys. Fluids **10**, 237 (1998)

Porter, D.H., Pouquet, A., Woodward, P.R.: Phys. Rev. Lett. **66**, 6301 (2002)

Roux, S., Muzy J.-F., Arnéodo, A.: Eur. Phys. J. B **8**, 301 (1999)

Scalo, J., Elmegreen, B.: Ann. Rev. Astron. Astrophys. **42**, 275 (2004)

Schmidt, W., Ciaraldi-Schoolmann, F., Niemeyer, J.C., Röpke, F.K., Hillebrandt, W.: Astrophys. J. **710**, 1683 (2010)

She, Z.-S., Lévêque, E.: Phys. Rev. **72**, 336 (1994)

Uritsky, V.M., Pouquet, A., Rosenberg, D., Mininni, P.D., Donovan, E.F.: Phys. Rev. E **82**, e6326 (2010)

Vestuto, J.G., Ostriker, E.C., Stone, J.M.: Astrophys. J. **590**, 858 (2003)

von Weizsäcker, C.F.: Astrophys. J. **114**, 165 (1951)

Wan, M., Oughton, S., Servidio, S., Matthaeus, W.H.: J. Fluid Mech. **697**, 296 (2012)